

Article

# Hybrid Nanofluid Slip Flow over an Exponentially Stretching/Shrinking Permeable Sheet with Heat Generation

Nur Syahirah Wahid <sup>1</sup>, Norihan Md Arifin <sup>1,2,\*</sup>, Naiyah Safwa Khashi'e <sup>3</sup> and Ioan Pop <sup>4</sup>

<sup>1</sup> Department of Mathematics, Faculty of Science, Universiti Putra Malaysia, UPM, Serdang 43400, Selangor, Malaysia; gs58394@student.upm.edu.my

<sup>2</sup> Institute for Mathematical Research, Universiti Putra Malaysia, UPM, Serdang 43400, Selangor, Malaysia

<sup>3</sup> Fakulti Teknologi Kejuruteraan Mekanikal dan Pembuatan, Universiti Teknikal Malaysia Melaka, Hang Tuah Jaya, Durian Tunggal 76100, Melaka, Malaysia; naiyah@utem.edu.my

<sup>4</sup> Department of Mathematics, Babeş-Bolyai University, R-400084 Cluj-Napoca, Romania; popm.ioan@yahoo.co.uk

\* Correspondence: norihana@upm.edu.my

**Abstract:** An investigation has been done on the hybrid nanofluid slip flow in the existence of heat generation over an exponentially stretching/shrinking permeable sheet. Hybridization of alumina and copper with water as the base fluid is considered. The mathematical model is simplified through the similarity transformation. A numerical solver named bvp4c in Matlab software is utilized to facilitate the problem-solving process and dual solutions are attained. The influences of several pertinent parameters on the main physical quantities of interest and the profiles are scrutinized and presented in the form of graphs. Through the stability analysis, only the first solution is considered as the physical solution. As such, the findings conclude that the upsurges of volume fraction on the copper nanoparticle could enhance the skin friction coefficient and the local Nusselt number.



**Citation:** Wahid, N.S.; Arifin, N.M.; Khashi'e, N.S.; Pop, I. Hybrid Nanofluid Slip Flow over an Exponentially Stretching/Shrinking Permeable Sheet with Heat Generation. *Mathematics* **2021**, *9*, 30. <https://dx.doi.org/10.3390/math9030030>

Received: 25 November 2020

Accepted: 19 December 2020

Published: 24 December 2020

**Publisher's Note:** MDPI stays neutral with regard to jurisdictional claims in published maps and institutional affiliations.



**Copyright:** © 2020 by the authors. Licensee MDPI, Basel, Switzerland. This article is an open access article distributed under the terms and conditions of the Creative Commons Attribution (CC BY) license (<https://creativecommons.org/licenses/by/4.0/>).

## 1. Introduction

Heat transfer becomes the most important process with the evolution of advanced technology. Applications and industries involving heat generation, such as manufacturing, thermal power generation, transportation, chemical processes and many others, necessitate an efficient heat transfer performance to produce the best outcome. Nanofluid applications have been thoroughly reviewed by Sidik et al. [1,2] and also by Huminic and Huminic [3]. Historically, various investigations have been conducted to improvise the heat transfer capability of the transferring medium which is perceived as a heat transfer fluid.

The idea of dispersing high-thermal conductivity solid particles of microsize into the conventional fluid was first pioneered by Maxwell [4] and then continued by Hamilton and Crosser [5] to intensify the fluid thermal conductivity. Nevertheless, some limitations and flaws still occurred, such as the coagulation in the fluid flow passage. Owing to that limitation, a rapid investigation is being made and nanofluid is established. Choi and Eastman [6] invented this novel heat transfer fluid by dispersing the nanometer-sized solid particles into the base fluid, and it is believed these could overcome the coagulation of the flow passage due to its special feature.

However, along with the development of technologies, another class of heat transfer fluid named hybrid nanofluid is established as the extension to nanofluid that is invented by the dispersion of dual or multiple kinds of nanosized solid particles with a good thermal conductivity into a base fluid. Looking through the reviews of the previous investigations by the researchers and scientists [7–11], hybrid nanofluid is claimed to have a preferable capability in terms of thermal conductivity and heat transfer due to its synergistic effects,

contrasted to mono nanofluid and regular fluid. Because of that, this new heat transfer fluid captivated many researchers and encouraged them to conduct further investigation into this fluid to understand its rheological properties and the mechanisms behind it, as well as to cope with the exponential growth demand of technology and science.

It seems like Devi and Devi [12–14] are among the earliest ones who discovered the flow of hybrid nanofluid at the boundary layer, mathematically and numerically, and their study emphasizes alumina and copper as the hybrid nanoparticles. Aly and Pop [15] considered hybrid nanofluid in their research into the flow and heat transfer over a stretching/shrinking sheet. They concluded that the hybrid nanofluid causes more reduction in the temperature profile unlike the mono nanofluid when the magnetic field, suction and copper volume fraction parameters are amplified. Waini et al. [16] also reported that the presence of a huge volume fraction of copper intensifies the skin friction coefficient and the local Nusselt number. Many other recent interesting investigations towards hybrid nanofluid, focusing on alumina and copper as the hybrid nanoparticles, with various configurations of parameters, have also been revealed by Yashkun et al. [17], Lund et al. [18,19], Aladdin et al. [20], Roşca et al. [21], Khashi'ie et al. [22–25], Roy and Pop [26], Zainal et al. [27], Anuar et al. [28], Gangadhar et al. [29] and Wahid et al. [30].

Slip condition is one of the parameters that is extensively being considered among the researchers and is significantly important in the heat transfer process. This condition happens when the fluid flow velocity is different from the velocity at the boundary. In industrial application, slip is significantly used in the microelectronic cooling system, micro heat exchangers, internal cavities' and artificial heart valves' polishing, and drug delivery system [31–33]. The presence of slip could reduce the resistance of the flow in microchannels and nanochannels as well as enhancing the efficiency of microscale viscous pumps. The appropriate degree of slip should be considered for the effectiveness of the applications that are also concerned with the other related parameters as well, thus various investigations towards the slip condition should be examined specifically. Presumably, Andersson [34] was the first one who examined the slip effect of the flow in the boundary layer of viscous fluid. In this regard, the investigation on the slip effect towards the hybrid nanofluid flow is still an ongoing research area. More recently, Hayat et al. [35] considered the partial slip on the Ag-CuO/H<sub>2</sub>O hybrid nanofluid due to rotating flow. They found out that the skin friction coefficient is lessened as the velocity slip is augmented in the case of the stretching sheet. Nadeem and Abbas [36] scrutinized the micropolar hybrid nanofluid with slip effect. A comparative investigation was made by Hayat et al. [37] on the hybrid and mono nanofluid of multi-walled carbon nanotubes with the slip flow. Yan et al. [38] elucidated the multiple slip conditions on the magnetized hybrid nanofluid with the consideration of a few other parameters. It was found out that thermal slip diminishes the heat transfer rate. Later, the velocity slip and temperature slip were simultaneously modeled by Alharbi [39] in the study of hybrid nanofluid and the influence of velocity slip is consistent with the result obtained by Hayat et al. [35]. Such other studies on slip conditions towards hybrid nanofluid were also reported by Tlili et al. [40], Aly and Pop [41] and Eid and Nafe [42]. The reported results in these investigations could provide the initial insight for the engineers and researchers needed to predict and control the slip parameter towards the related applied area.

Besides this, heat generation/absorption also becomes an essential aspect when managing the performance of the heat transfer. Due to that, investigations into the effects of heat generation/absorption towards nanofluid have been carried out up until now. Abbas et al. [43] contemplated the slip flow of nanofluids with heat generation due to the curved stretching surface. Upreti et al. [44] explored the heat generation of nanofluids due to the flat porous plate. Jusoh et al. [45] elaborated on the nanofluid stagnation point flow with heat generation. Murugesan and Kumar [46] also elucidated the same effect but with the flow of nanofluid over the exponentially stretching sheet. With the evolution of nanofluid to hybrid nanofluid, this heat generation/absorption effect has been considered by Hayat and Nadeem [47] with regard to the model of hybrid nanofluid with the three-dimensional

flow, which was then continued by Hayat et al. [48], who analyzed such effects on the rotating hybrid nanofluid. Eid and Nafe [42] also considered the presence of heat generation together with the slip effect in their research on hybrid nanofluid. Most of them indicated that the amplification of heat generation increases the temperature profile.

Therefore, in this present study, we intended to scrutinize the slip flow and heat transfer of a hybrid nanofluid of alumina and copper (hybrid nanoparticles) with water (base fluid) over an exponentially permeable stretching/shrinking sheet with the consideration of heat generation. Both velocity and thermal slips are being considered in the model. We believe the model of a hybrid nanofluid with such configurated effects and surface is still not being explored by the researchers, judging by the previous literature. The influences of various parameters over the main physical quantities are provided in the figure of the graph, and are discussed. An analysis of flow stability is also conducted, as the non-unique solutions are visible and the least eigenvalues that imply the stability of the flow are tabulated.

## 2. Mathematical Formulation

A steady boundary layer of hybrid nanofluid slip flow induced by an exponentially permeable stretching/shrinking sheet with heat generation is scrutinized. According to the physical model in Figure 1,  $u$  and  $v$  are the elements of velocity in  $x$  and  $y$  directions, respectively. The surface velocity is given as  $u_w(x) = ce^{x/L}$  and the wall mass transfer velocity is specified as  $v_w(x) = v_0e^{x/2L}$  ( $v_0 < 0$  is the mass suction and  $v_0 > 0$  is the mass injection),  $\lambda > 0$  is the stretching constant,  $\lambda < 0$  is the shrinking constant,  $\lambda = 0$  refers to a motionless sheet,  $T$  is temperature,  $T_w = T_\infty + T_0e^{x/2L}$  is the sheet of varying temperature with constant  $T_0$  and  $q = q_0e^{x/L}$  is the heat generation rate constant.

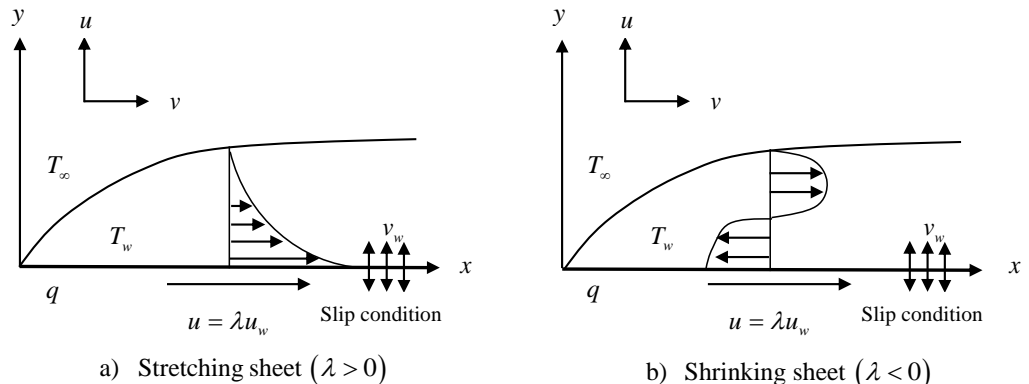


**Figure 1.** Physical model.

Therefore, concerning the mentioned boundary layer assumptions, the equations of continuity, momentum and energy are formulated as (Murugesan and Kumar [46], Ghosh and Mukhopadhyay [49], Waini et al. [16], Devi and Devi [14], Eid and Nafe [42])

$$\frac{\partial u}{\partial x} + \frac{\partial v}{\partial y} = 0 \quad (1)$$

$$u \frac{\partial u}{\partial x} + v \frac{\partial v}{\partial y} = \frac{\mu_{hnf}}{\rho_{hnf}} \frac{\partial^2 u}{\partial y^2} \quad (2)$$

$$u \frac{\partial T}{\partial x} + v \frac{\partial T}{\partial y} = \frac{k_{hnf}}{(\rho C_p)_{hnf}} \frac{\partial^2 T}{\partial y^2} + \frac{q}{(\rho C_p)_{hnf}} (T - T_\infty) \quad (3)$$

due to the boundary conditions (Ghosh and Mukhopadhyay [49], Mukhopadhyay and Andersson [50])

$$\begin{aligned} u &= u_w(x)\lambda + A_1 \frac{\mu_{hnf}}{\rho_{hnf}} \frac{\partial u}{\partial y}, \quad v = v_w, \quad T = T_w(x) + B_1 \frac{\partial T}{\partial y} \text{ at } y = 0 \\ u &\rightarrow 0, \quad T \rightarrow T_\infty \text{ as } y \rightarrow \infty \end{aligned} \quad (4)$$

in which  $A_1$  and  $B_1$  are the slip factors for velocity and thermal, respectively. The correlation of the physical properties (Tayebi and Chamkha [51], Takabi and Salehi [52], Babu et al. [11], Ghalambaz et al. [53]) and the hybrid nanofluid's thermo-physical properties (Oztop and Abu-Nada [54]) is depicted in Tables 1 and 2, respectively. Here, the  $hnf$ ,  $f$ ,  $s1$  and  $s2$  subscripts refer to the hybrid nanofluid, base fluid and solid nanoparticle for the alumina and solid nanoparticle for copper, accordingly, and  $\phi_{s1}$  and  $\phi_{s2}$  symbolize the alumina and copper volume fraction parameters, separately.

**Table 1.** Hybrid nanofluid physical properties.

Properties	Hybrid Nanofluid Correlations
Density	$\rho_{hnf} = \rho_{s1}\phi_{s1} + \rho_{s2}\phi_{s2} + \rho_f(1 - \phi_{hnf})$ where $\phi_{hnf} = \phi_{s1} + \phi_{s2}$
Heat Capacity	$(\rho C_p)_{hnf} = (\rho C_p)_{s1}\phi_{s1} + (\rho C_p)_{s2}\phi_{s2} + (\rho C_p)_f(1 - \phi_{hnf})$
Dynamic Viscosity	$\frac{\mu_{hnf}}{\mu_f} = \frac{1}{(1 - \phi_{hnf})^{2.5}}$
Thermal Conductivity	$\frac{k_{hnf}}{k_f} = \left[ \frac{2k_f + \left( \frac{\phi_{s1}k_{s1} + \phi_{s2}k_{s2}}{\phi_{hnf}} \right) + 2(\phi_{s1}k_{s1} + \phi_{s2}k_{s2}) - 2\phi_{hnf}k_f}{2k_f - (\phi_{s1}k_{s1} + \phi_{s2}k_{s2}) + \left( \frac{\phi_{s1}k_{s1} + \phi_{s2}k_{s2}}{\phi_{hnf}} \right) + \phi_{hnf}k_f} \right]$

**Table 2.** Thermo-physical properties.

Physical Properties	Water	Al <sub>2</sub> O <sub>3</sub>	Cu
$\rho$ (kg/m <sup>3</sup> )	997.1	3970	8933
$C_p$ (J/kgK)	4179	765	385
$k$ (W/mK)	0.613	40	400

As to reduce the aforementioned governing equations, the similarity variables are employed (Waini et al. [16], Eid and Nafe [42])

$$\psi = e^{x/2L} \sqrt{2\nu_f L c f}(\eta), \quad u = \frac{\partial \psi}{\partial y}, \quad v = -\frac{\partial \psi}{\partial x}, \quad \theta(\eta) = \frac{T - T_\infty}{T_w - T_\infty}, \quad \eta = y e^{x/2L} \sqrt{\frac{c}{2\nu_f L}} \quad (5)$$

which consequently gratify Equation (1) and transform Equations (2) and (3) into the subsequent equations

$$\left( \frac{\mu_{hnf}/\mu_f}{\rho_{hnf}/\rho_f} \right) f''' + ff'' - 2f'^2 = 0 \quad (6)$$

$$\frac{1}{Pr} \left( \frac{k_{hnf}}{k_f} \right) \theta'' + \frac{(\rho C_p)_{hnf}}{(\rho C_p)_f} (f\theta' - f'\theta) + \beta\theta = 0 \quad (7)$$

due to the transformed boundary conditions

$$\begin{aligned} f(0) &= S, \quad f'(0) = \lambda + Af''(0), \quad \theta(0) = 1 + B\theta'(0) \\ f'(\eta) &\rightarrow 0, \quad \theta(\eta) \rightarrow 0 \text{ as } \eta \rightarrow \infty \end{aligned} \quad (8)$$

such that  $\text{Pr} = (\mu C_p)_f/k_f$  is the Prandtl number,  $\beta = 2q_0L/c(\rho C_p)_f$  is the heat generation parameter,  $A = A_1(\mu_{hnf}/\rho_{hnf})e^{x/2L}\sqrt{c/2\nu_f L}$  is the dimensionless velocity slip parameter and  $B = B_1e^{x/2L}\sqrt{c/2\nu_f L}$  is the dimensionless thermal slip parameter, and  $S = -v_0/\sqrt{\nu_f c/2L}$  is the wall mass transfer parameter in which  $S > 0$  ( $v_0 < 0$ ) equates to mass suction and  $S < 0$  ( $v_0 > 0$ ) equates to mass injection.

The main physical quantities of interest (local skin friction coefficient  $C_f$  and the local Nusselt number  $Nu_x$ ) are mathematically computed as (Waini et al. [16], Eid and Nafe [42])

$$C_f = \frac{\mu_{hnf}}{\rho_f} \frac{1}{u^2 w} \left( \frac{\partial u}{\partial y} \right)_{y=0}, \quad Nu_x = \frac{k_{hnf}}{k_f} \frac{-2L}{(T_w - T_\infty)} \left( \frac{\partial T}{\partial y} \right)_{y=0} \quad (9)$$

or by introducing the transform, we have

$$\text{Re}_x^{1/2} C_f = \left( \frac{\mu_{hnf}}{\mu_f} \right) f''(0), \quad \text{Re}_x^{-1/2} Nu_x = - \left( \frac{k_{hnf}}{k_f} \right) \theta'(0) \quad (10)$$

where  $\text{Re}_x = 2Lu_w/\nu_f$  is the local Reynolds number.

### 3. Flow Stability

As it is attainable to compute dual solutions, the flow stability analysis is executed. The problem is regarded as unsteady in this analysis where the continuity equation (Equation (1)) is held, and the time derivative is introduced to Equations (2) and (3)

$$u \frac{\partial u}{\partial x} + v \frac{\partial u}{\partial y} + \frac{\partial u}{\partial t} = \frac{\mu_{hnf}}{\rho_{hnf}} \frac{\partial^2 u}{\partial y^2} \quad (11)$$

$$u \frac{\partial T}{\partial x} + v \frac{\partial T}{\partial y} + \frac{\partial T}{\partial t} = \frac{k_{hnf}}{(\rho C_p)_{hnf}} \frac{\partial^2 T}{\partial y^2} + \frac{q}{(\rho C_p)_{hnf}} (T - T_\infty) \quad (12)$$

where the variable  $t$  here denotes time.

Referencing the work reported by Merkin [55], Weidman et al. [56], Waini et al. [16] and Yan et al. [38], the dimensionless time-dependent variable transformation for Equations (11) and (12) is

$$\eta = ye^{x/2L} \sqrt{\frac{c}{2\nu_f L}}, \quad \psi = f(\eta, \tau) e^{x/2L} \sqrt{2\nu_f L c}, \quad \theta(\eta, \tau) = \frac{T - T_\infty}{T_w - T_\infty}, \quad \tau = \frac{c}{2L} te^{x/L} \quad (13)$$

As such, with the utilization of the transformation, the subsequent equations are procured

$$\left( \frac{\mu_{hnf}/\mu_f}{\rho_{hnf}/\rho_f} \right) \frac{\partial^3 f}{\partial \eta^3} + \frac{\partial^2 f}{\partial \eta^2} f - 2 \left( \frac{\partial f}{\partial \eta} \right)^2 - \frac{\partial^2 f}{\partial \eta \partial \tau} = 0 \quad (14)$$

$$\frac{1}{\text{Pr}} \left( \frac{k_{hnf}}{k_f} \right) \frac{\partial^2 \theta}{\partial \eta^2} + \frac{(\rho C_p)_{hnf}}{(\rho C_p)_f} \left( \frac{\partial \theta}{\partial \eta} f - \theta \frac{\partial f}{\partial \eta} - \left( \frac{\partial \theta}{\partial \tau} \right) \right) + \beta \theta = 0 \quad (15)$$

restricted to the conditions

$$f(0, \tau) = S, \quad \frac{\partial f}{\partial \eta}(0, \tau) = \lambda + A \frac{\partial^2 f}{\partial \eta^2}(0, \tau), \quad \theta(0) = 1 + B \frac{\partial \theta}{\partial \eta}(0, \tau) \\ \frac{\partial f}{\partial \eta}(\eta, \tau) \rightarrow 0, \quad \theta(\eta, \tau) \rightarrow 0 \text{ as } \eta \rightarrow \infty \quad (16)$$

The succeeding perturbation equation is introduced for the stability analysis of the similarity solutions,  $f(\eta) = f_0(\eta)$  and  $\theta(\eta) = \theta_0(\eta)$ ,

$$\begin{aligned} f(\eta, \tau) &= f_0(\eta) + e^{-\gamma\tau} F(\eta) \\ \theta(\eta, \tau) &= \theta_0(\eta) + e^{-\gamma\tau} G(\eta) \end{aligned} \quad (17)$$

where  $\gamma$  is an unidentified eigenvalue, while  $F(\eta)$  and  $G(\eta)$  are small relative to  $f_0(\eta)$  and  $\theta_0(\eta)$ , correspondingly (Weidman et al. [56], Waini et al. [16], Yan et al. [38]).

Substituting Equation (17) into Equations (14)–(16) and setting the value of  $\tau$  to zero, the initial decay or growth of disturbance in Equation (17) can be identified and the subsequent linearized equations are attained

$$\left( \frac{\mu_{hnf}/\mu_f}{\rho_{hnf}/\rho_f} \right) F''' + f_0'' F + F'' f_0 - 4f_0' F' + \gamma F' = 0 \quad (18)$$

$$\frac{1}{Pr} \left( \frac{k_{hnf}}{k_f} \right) G'' + \frac{(\rho C_p)_{hnf}}{(\rho C_p)_f} (\theta_0' F + G' f_0 - \theta_0 F' - G f_0' + \gamma G) + \beta G = 0 \quad (19)$$

subject to the linearized conditions

$$\begin{aligned} F(0) &= 0, F'(0) = AF''(0), G(0) = BG'(0) \\ F'(\infty) &\rightarrow 0, G(\infty) \rightarrow 0 \end{aligned} \quad (20)$$

Since most of the linearized conditions (Equation (20)) are equal to zero, it is essential for  $F'(\infty) \rightarrow 0$  to relax and be replaced with  $F''(0) = 1$  to produce a realizable range of eigenvalues. Thus, to attain the unknown eigenvalues  $\gamma$  which act as the indicator to ascertain the stability of the flow, the bvp4c solver is utilized. The flow is contemplated to be stable when  $\gamma > 0$ , and vice versa.

#### 4. Result and Discussions

The solutions for Equations (6) and (7) conditioned to Equation (8) are numerically enumerated by employing the bvp4c solver in Matlab software. The suitable preliminary guesses, preferable boundary layer thickness and various values of parameters need to be selected and well-adjusted in the coding function of the solver to compute the most precise results. Stretching ( $\lambda > 0$ ) and shrinking ( $\lambda < 0$ ) surfaces are considered in this study. The Prandtl number and nanoparticle volume fraction for alumina are specified to be fixed throughout this study as  $Pr = 6.2$  and  $\phi_{s1} = 0.01$ , respectively, while the other parameters, such as velocity  $A$  and thermal  $B$  slips, nanoparticle volume fraction for copper  $\phi_{s2}$ , heat generation  $\beta$  and suction  $S$ , are set to be varied in order to study their impacts with regard to the boundary layer flow and heat transfer.

For verification purposes, the results presented in this study are contrasted with the past results revealed by Ghosh and Mukhopadhyay [49], Hafidzuddin et al. [57] and Waini et al. [16]. The numerical values of  $f''(0)$  and  $-\theta'(0)$  are computed and compared in Table 3 for the case of viscous fluid ( $\phi_{s1} = \phi_{s2} = 0$ ) and shrinking surface ( $\lambda = -1$ ) with  $S = 3$  and  $Pr = 0.7$ . We observe that the present and previous results are found to be in a reasonable correlation. Thus, we guarantee that the technique, as well as the results provided in this present study, are valid and acceptable.

**Table 3.** Tabulation of  $f''(0)$  and  $-\theta'(0)$  for viscous fluid ( $\phi_{s1} = \phi_{s2} = 0$ ) when  $\text{Pr} = 0.7$ ,  $S = 3$  and  $A = B = \beta = 0$  for the shrinking surface ( $\lambda = -1$ ) case.

	$f''(0)$		$-\theta'(0)$	
	First Solution	Second Solution	First Solution	Second Solution
Ghosh and Mukhopadhyay [49]	2.39082	-0.97223	1.7712	0.84832
Hafidzuddin et al. [57]	2.3908	-0.9722	1.7712	0.8483
Waini et al. [16]	2.390814	-0.972247	1.771237	0.848316
Present Results	2.390813634	-0.972128868	1.771237307	0.847748272

The non-unique or the dual solutions of Equations (6) and (7) are perceived to exist in this study for certain values of parameters, as can be observed in Figures 2–9 for the plots of skin friction coefficient  $\text{Re}_x^{1/2}C_f$  and the local Nusselt number  $\text{Re}_x^{-1/2}Nu_x$ , and also in Figures 10–17 for the plots of velocity and temperature profiles. The plots of the skin friction coefficient  $\text{Re}_x^{1/2}C_f$  and local Nusselt number  $\text{Re}_x^{-1/2}Nu_x$  against the stretching/shrinking parameter  $\lambda$ , with varied values of velocity slip parameter  $A$  ( $= 0.2, 0.4, 0.6$ ) when  $S = 2.4$ ,  $\phi_{s2} = 0.01$ ,  $B = 0.2$  and  $\beta = 0.02$ , are exhibited in Figures 2 and 3. It is discovered from the figures that the presence of dual solutions is visible for  $A = 0.2, 0.4, 0.6$  when  $\lambda_{c1} = -1.4419$ ,  $\lambda_{c2} = -1.7322$ ,  $\lambda_{c3} = -2.0362$  respectively. This also indicates that the bifurcation point of the boundary layer only appears at the shrinking surface ( $\lambda < 0$ ) region and the surges of velocity slip parameter  $A$  delay the bifurcation of the boundary layer.

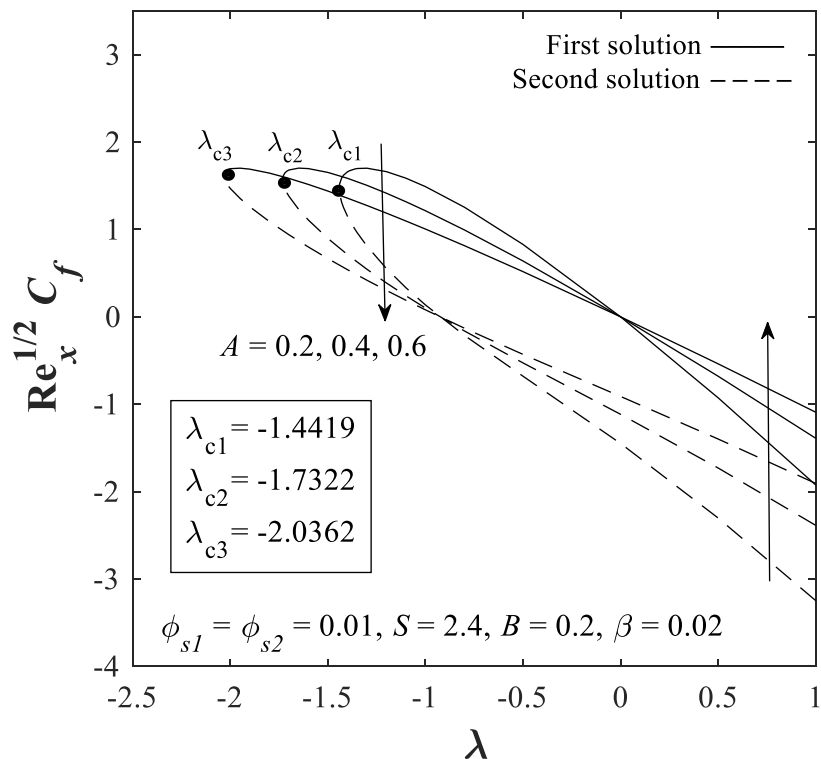


**Figure 2.** Plot of  $\text{Re}_x^{1/2}C_f$  with  $\lambda$  for varied  $A$ .

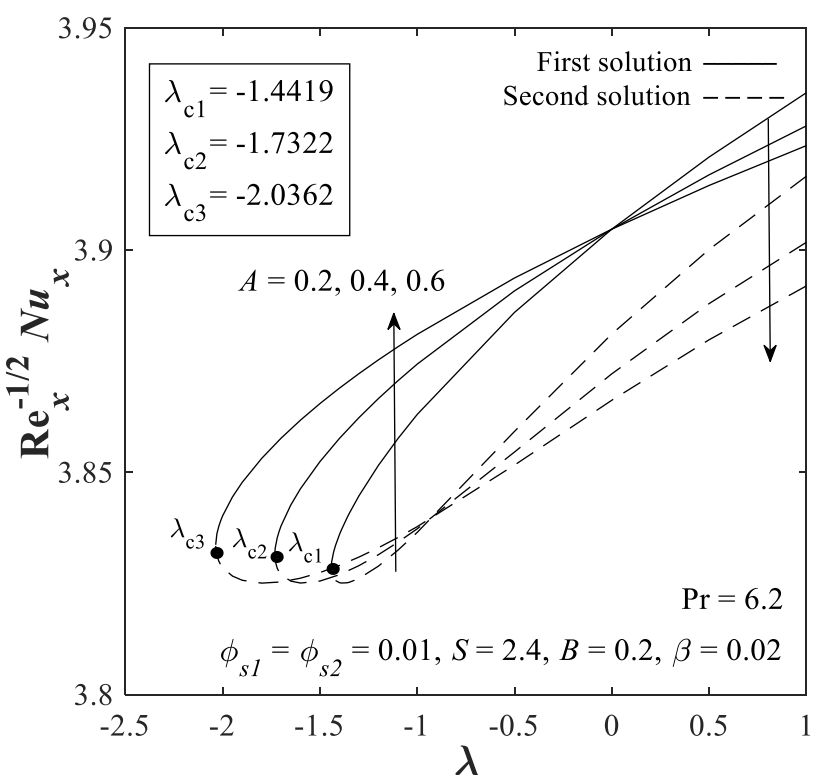


**Figure 3.** Plot of  $\text{Re}_x^{-1/2} \text{Nu}_x$  with  $\lambda$  for varied  $A$ .

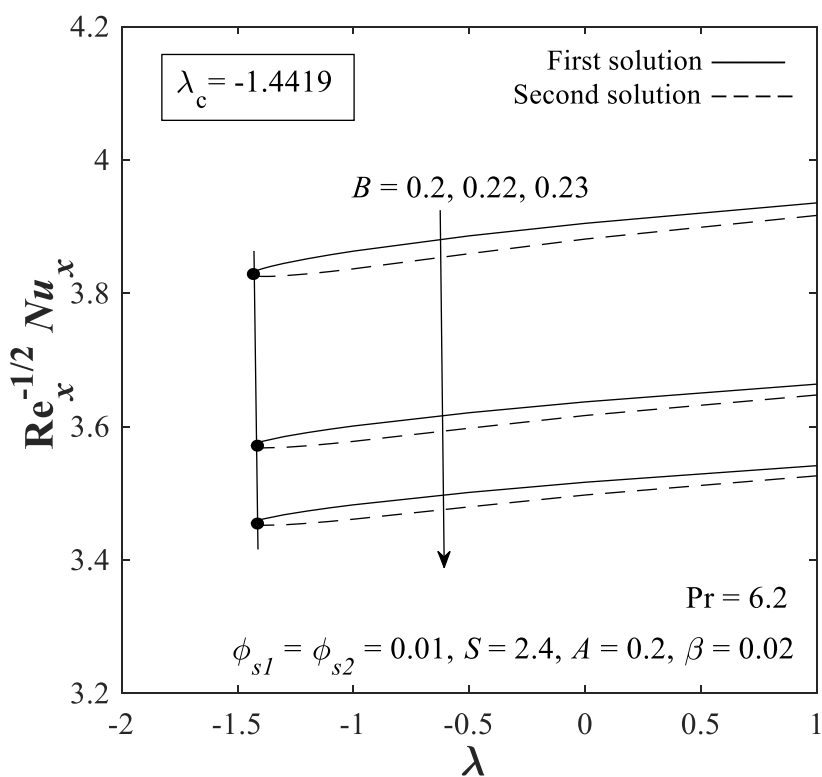


**Figure 4.** Plot of  $\text{Re}_x^{-1/2} \text{Nu}_x$  with  $\lambda$  for varied  $B$ .

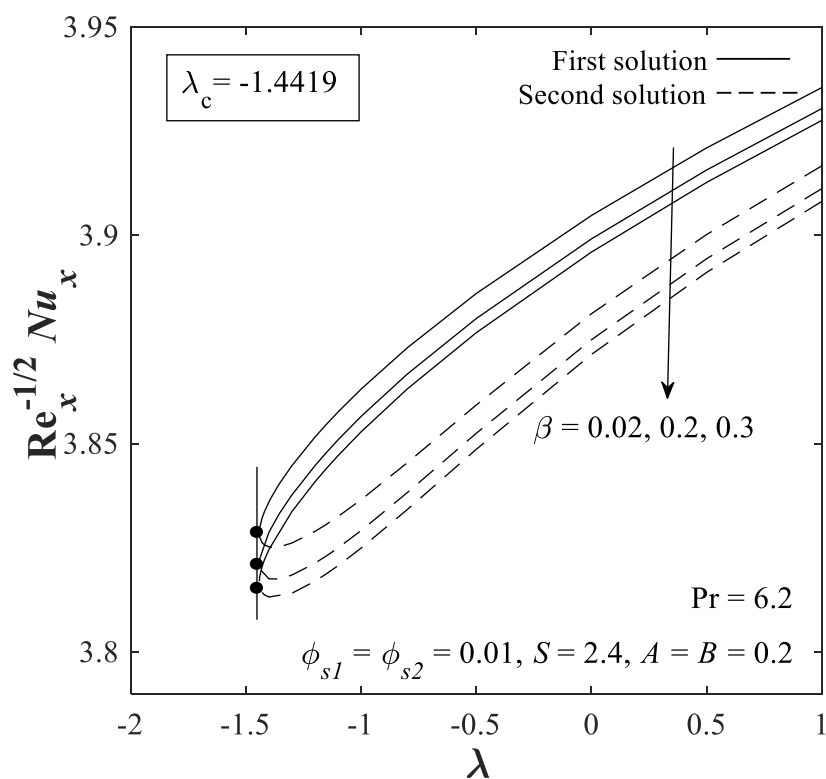


**Figure 5.** Plot of  $\text{Re}_x^{-1/2} \text{Nu}_x$  with  $\lambda$  for varied  $\beta$ .

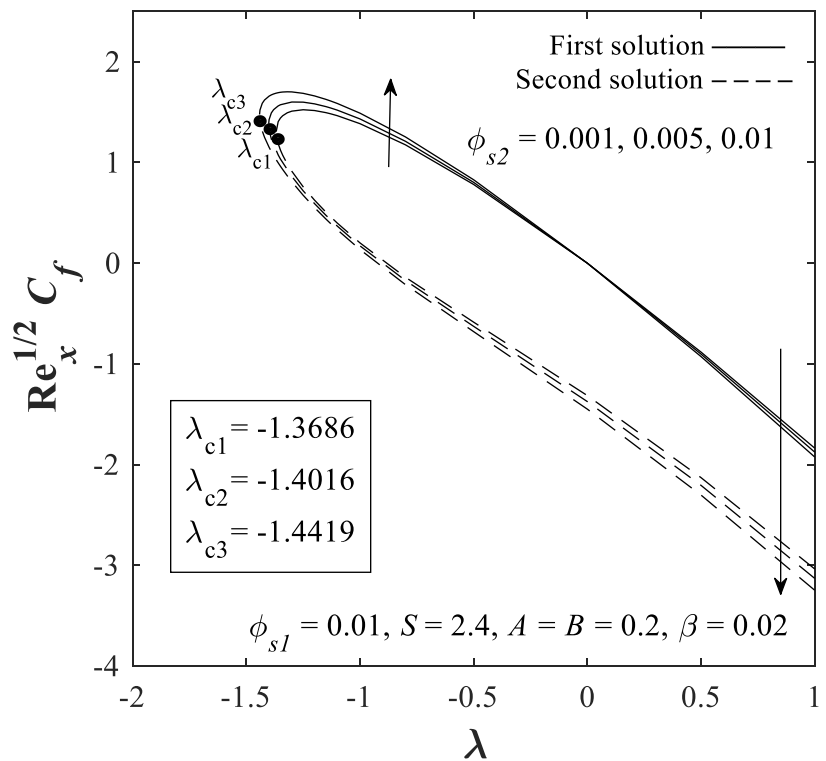


**Figure 6.** Plot of  $\text{Re}_x^{1/2} C_f$  with  $\lambda$  for varied  $\phi_{s2}$ .

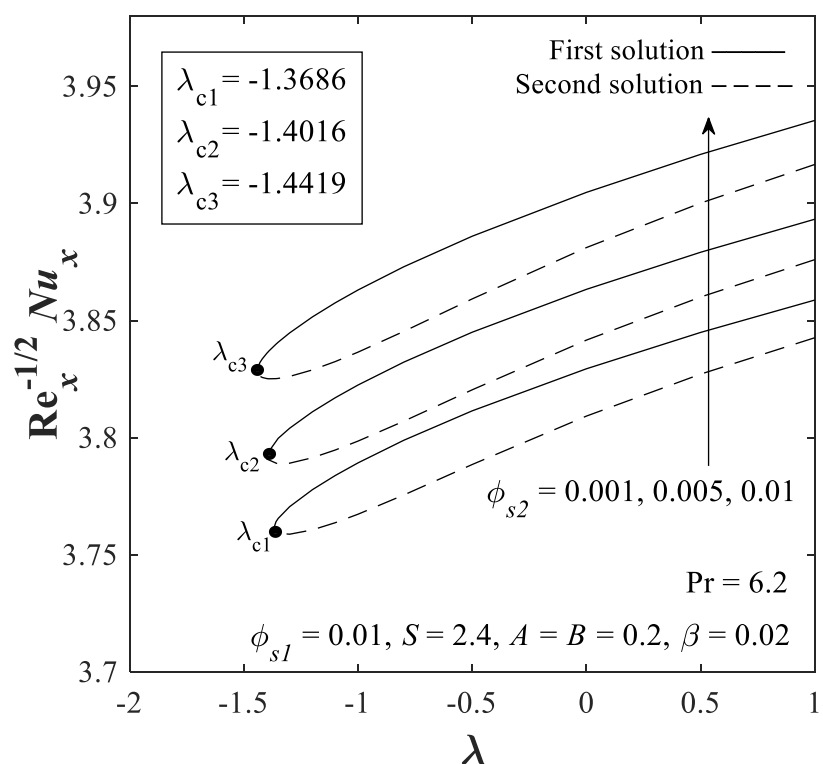


**Figure 7.** Plot of  $\text{Re}_x^{-1/2} \text{Nu}_x$  with  $\lambda$  for varied  $\phi_{s2}$ .

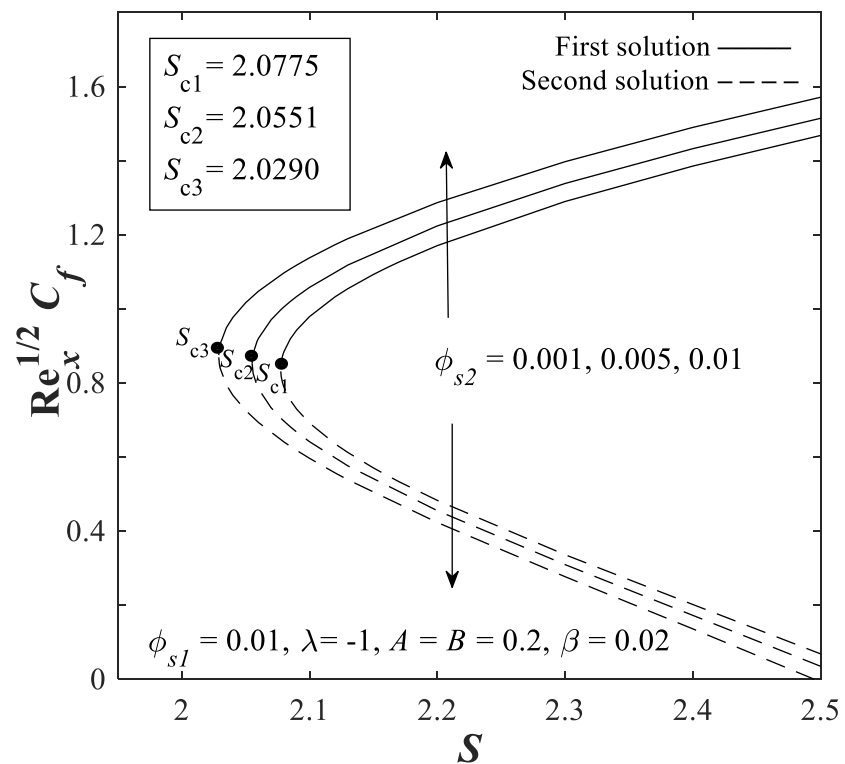


**Figure 8.** Plot of  $\text{Re}_x^{1/2} C_f$  with  $S$  for varied  $\phi_{s2}$ .

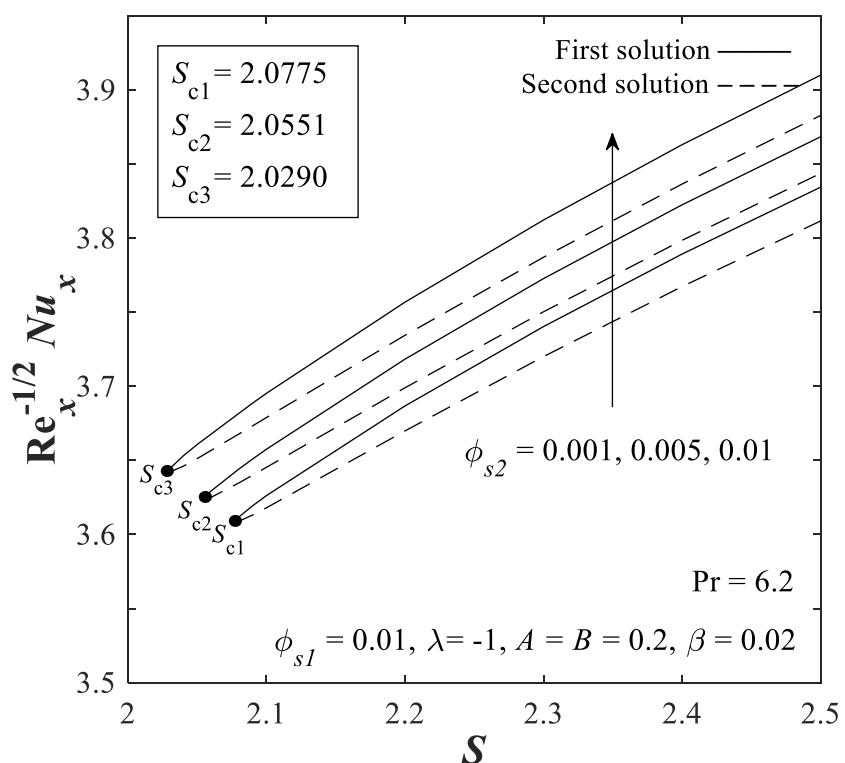


**Figure 9.** Plot of  $\text{Re}_x^{-1/2} \text{Nu}_x$  with  $S$  for varied  $\phi_{s2}$ .

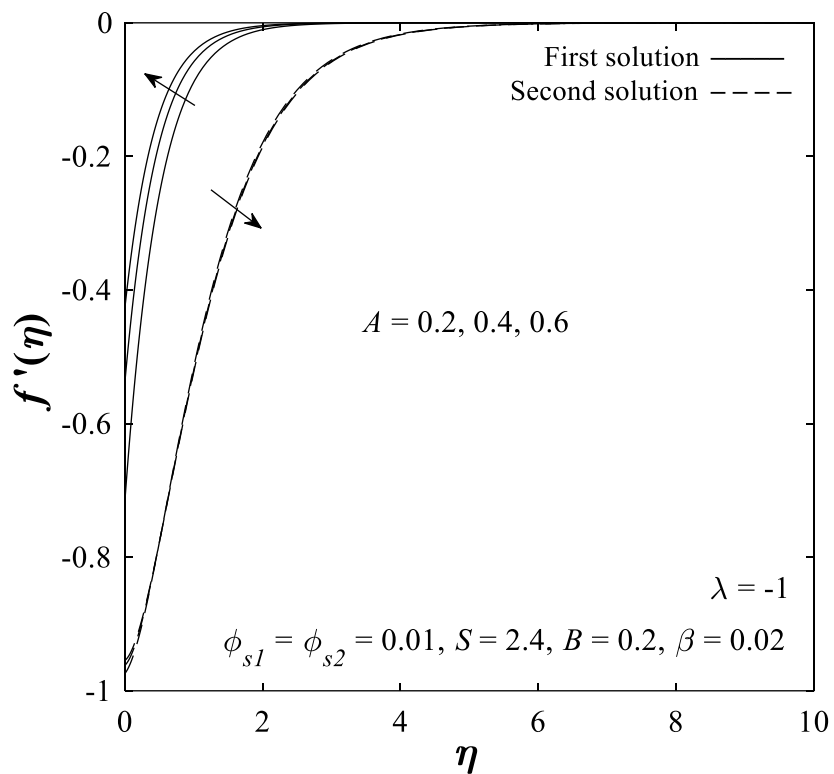


**Figure 10.** Velocity profile  $f'(\eta)$  for varied  $A$ .

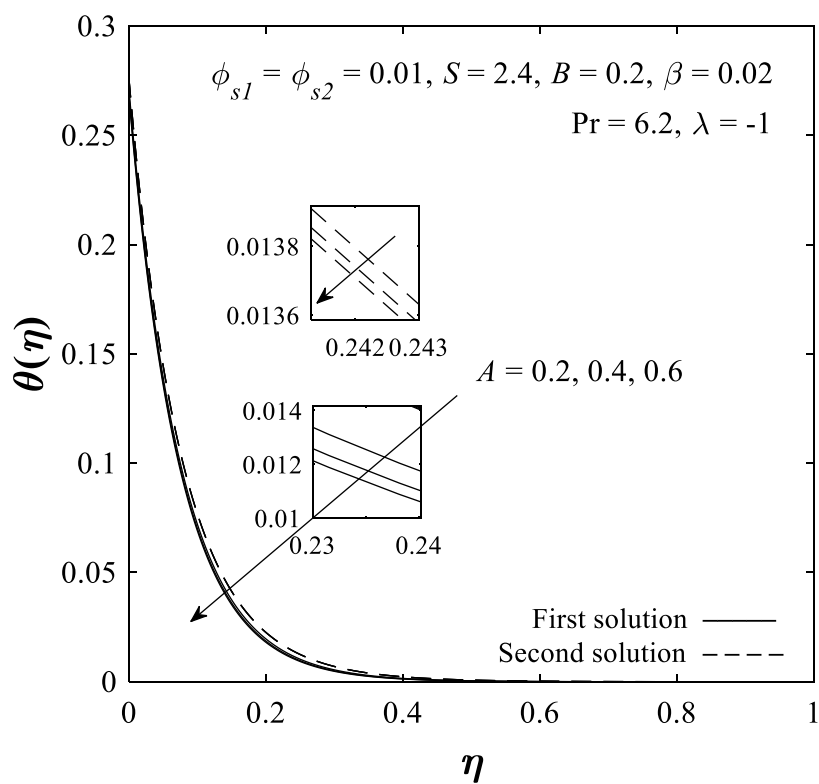


**Figure 11.** Temperature profile  $\theta(\eta)$  for varied  $A$ .

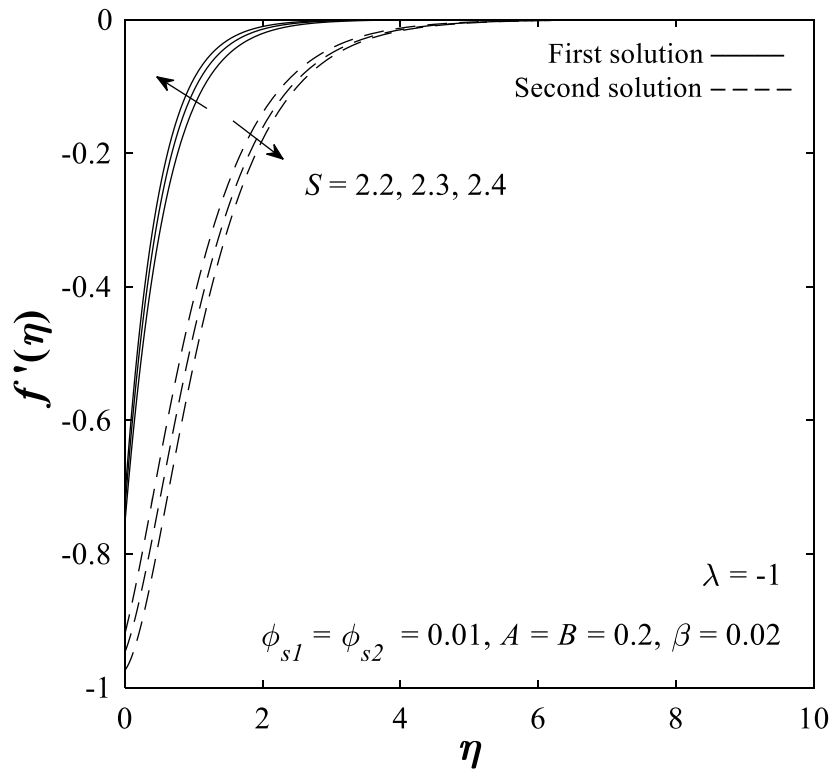


**Figure 12.** Velocity profile  $f'(\eta)$  for varied  $S$ .

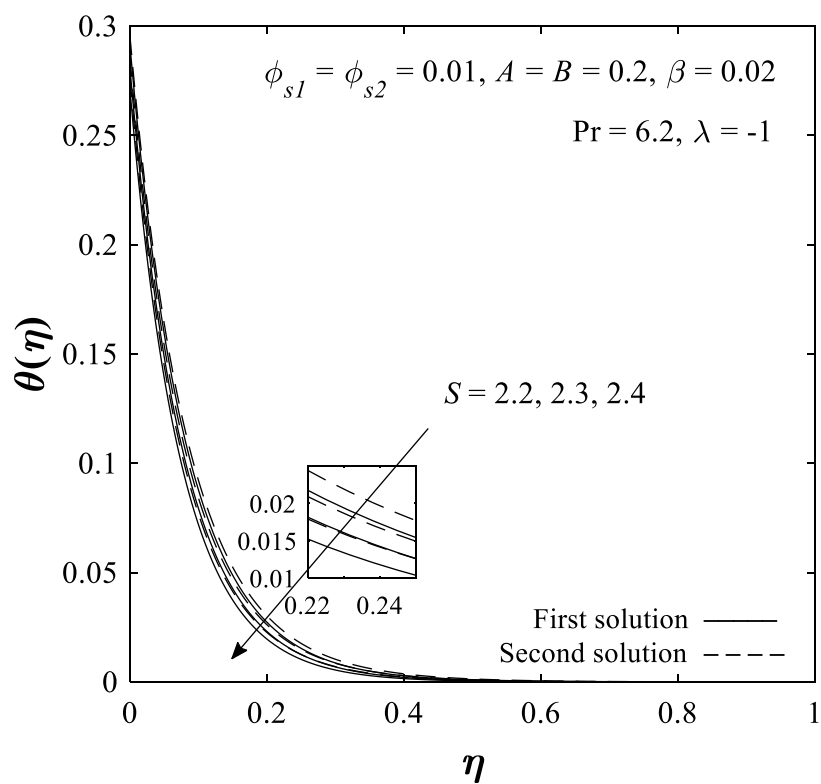


**Figure 13.** Temperature profile  $\theta(\eta)$  for varied  $S$ .

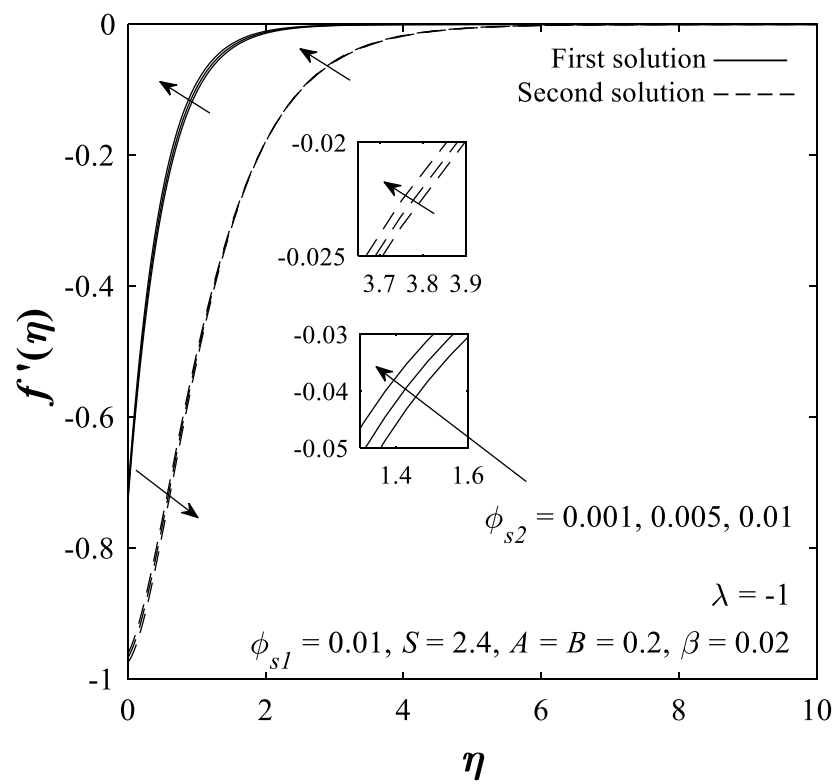


**Figure 14.** Velocity profile  $f'(\eta)$  for varied  $\phi_{s2}$ .

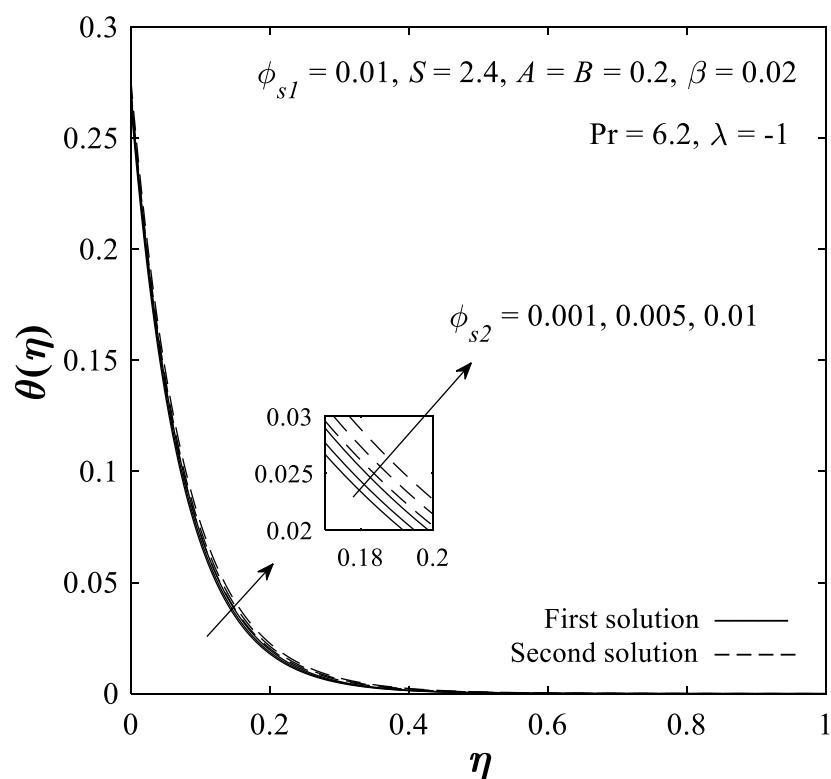


Figure 15. Temperature profile  $\theta(\eta)$  for varied  $\phi_{s2}$ .

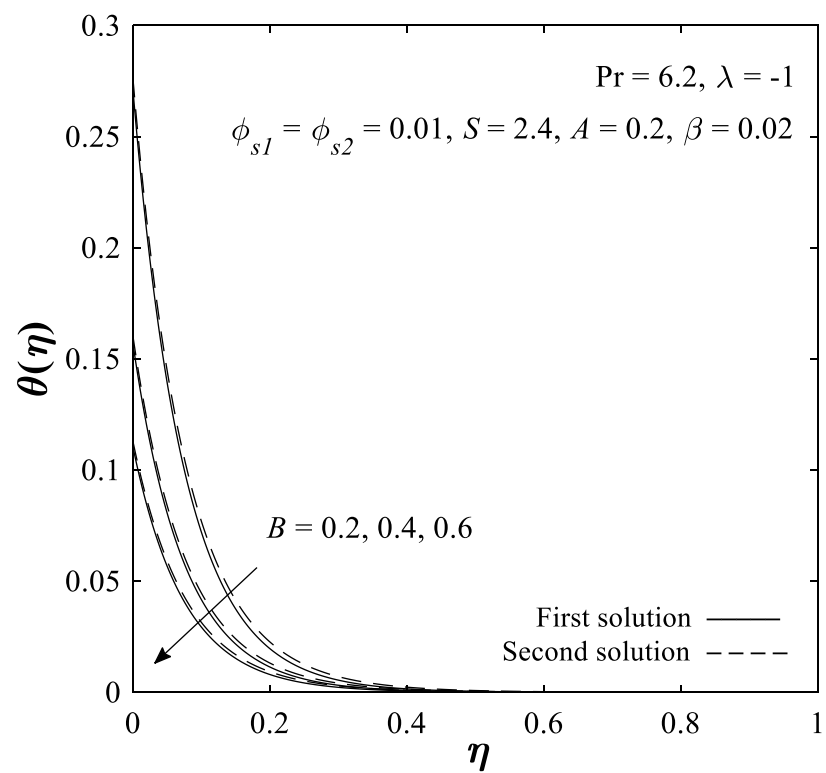
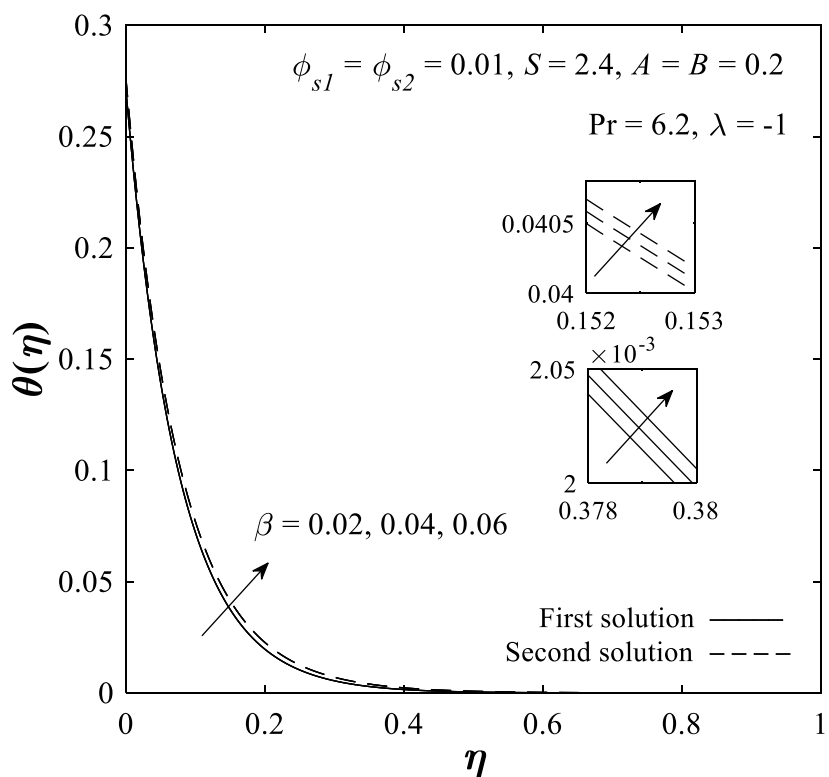


Figure 16. Temperature profile  $\theta(\eta)$  for varied  $B$ .



**Figure 17.** Temperature profile  $\theta(\eta)$  for varied  $\beta$ .

In Figure 2, the skin friction coefficient  $Re_x^{1/2} C_f$  is noted to be in a decreasing trend as the velocity slip parameter  $A$  escalates for the first solution in a certain range ( $-1.4419 \leq \lambda < 0$ ) in the shrinking surface ( $\lambda < 0$ ) region, but the opposite trend occurs when approaching the stretching surface ( $\lambda > 0$ ) region and onwards. However, for the local Nusselt number  $Re_x^{-1/2} Nu_x$ , it is noticed from Figure 3 that the enhancement in the value of the velocity slip parameter  $A$  promotes the increment in the local Nusselt number  $Re_x^{-1/2} Nu_x$  for the first solution, but when approaching the stretching surface ( $\lambda > 0$ ) region, the opposite trend occurs. Meanwhile, for the second solution of the skin friction coefficient  $Re_x^{1/2} C_f$  and the local Nusselt number  $Re_x^{-1/2} Nu_x$ , a similar trend is also noticed to occur like the first solution, but a change of trend happens within a certain range of shrinking surface ( $\lambda < 0$ ) region and the stretching surface region ( $\lambda > 0$ ) onwards, unlike in the first solution. The skin friction coefficient  $Re_x^{1/2} C_f$  is also perceived to increase as the value of the stretching/shrinking parameter  $\lambda$  diminishes, while the obverse occurs for the local Nusselt number  $Re_x^{-1/2} Nu_x$  for both the first and second solutions.

The effects of the thermal slip and heat generation parameters only impact the local Nusselt number  $Re_x^{-1/2} Nu_x$ . The plot of the local Nusselt number  $Re_x^{-1/2} Nu_x$  against the stretching/shrinking parameter  $\lambda$  for varied values of thermal slip  $B$  ( $= 0.2, 0.22, 0.23$ ) and heat generation  $\beta$  ( $= 0.02, 0.2, 0.3$ ) when  $S = 2.4$ ,  $\phi_{s2} = 0.01$  and  $A = 0.2$  is displayed in Figures 4 and 5. Dual solutions are observed to exist, starting at almost the same critical values for the varied values of both the thermal slip  $B$  and heat generation  $\beta$  parameters, which are  $\lambda_c = -1.4419$ . The existence of the thermal slip  $B$  and heat generation  $\beta$  parameters causes the local Nusselt number  $Re_x^{-1/2} Nu_x$  to decrease, but it is seen to increase as the stretching/shrinking parameter rises  $\lambda$  for both the first and second solutions.

Moreover, for the influence of copper volume fraction  $\phi_{s2}$  ( $= 0.001, 0.005, 0.01$ ) over the skin friction coefficient  $Re_x^{1/2} C_f$ , and the local Nusselt number  $Re_x^{-1/2} Nu_x$  against the stretching/shrinking parameter  $\lambda$  when  $S = 2.4$ ,  $A = B = 0.2$ ,  $\beta = 0.02$ , is shown in Figures 6 and 7, and the same against the suction parameter  $S$  when  $\lambda = -1$ ,  $A = B = 0.2$ ,  $\beta = 0.02$  is shown in Figures 8 and 9. It is noted that in Figures 6 and 7, the existence of dual solutions is visible for  $\phi_{s2}$  ( $= 0.001, 0.005, 0.01$ ) when  $\lambda_{c1} = -1.3686$ ,  $\lambda_{c2} = -1.4016$ ,

$\lambda_{c3} = -1.4419$ , which indicates that the bifurcation point of the boundary layer eventuates at the shrinking surface ( $\lambda < 0$ ) region and the presence of the copper volume fraction delays the bifurcation of the boundary layer.

The upsurge in the copper volume fraction parameter  $\phi_{s2}$  leads to the increase in the skin friction coefficient  $Re_x^{1/2}C_f$  at the shrinking surface ( $\lambda < 0$ ) region for the first solution, but leads to a reduction for the second solution. We also notice a change in the trend of the skin friction coefficient  $Re_x^{1/2}C_f$  for the first solution towards the copper volume fraction parameter  $\phi_{s2}$  when  $\lambda > 0$ . Meanwhile, the plot of the local Nusselt number  $Re_x^{-1/2}Nu_x$  is observed to rise when there is an upsurge in the copper volume fraction parameter  $\phi_{s2}$  for the first and second solutions. The plots of the skin friction coefficient  $Re_x^{1/2}C_f$  and local Nusselt number  $Re_x^{-1/2}Nu_x$  are noticed to increase and decrease, respectively, when the stretching/shrinking parameter  $\lambda$  decreases for both solutions.

In Figures 8 and 9, dual solutions are perceived to exist for  $\phi_{s2}$  ( $= 0.001, 0.005, 0.01$ ) when  $S_{c1} = 2.0775$ ,  $S_{c2} = 2.0551$ ,  $S_{c3} = 2.0290$ , which indicates that only certain appropriate values of suction are required to achieve dual solutions for the shrinking surface. In these figures, the increases in copper volume fraction  $\phi_{s2}$  and suction  $S$  parameters augment the skin friction coefficient  $Re_x^{1/2}C_f$  for the first solution but reduce the skin friction coefficient  $Re_x^{1/2}C_f$  for the second solution. Concurrently, the local Nusselt number  $Re_x^{-1/2}Nu_x$  is noted to augment when the copper volume fraction  $\phi_{s2}$  and suction  $S$  parameters increase for both of the solutions. From all of the figures (Figures 2–9), we noted that the plots of the skin friction coefficient and the local Nusselt number against both the stretching/shrinking and the suction parameters are all moving towards the left side of the domain, either up or down on the left side, to achieve the critical point.

The velocity  $f'(\eta)$  and temperature  $\theta(\eta)$  profiles are also provided as in Figures 10–17. The increment of velocity slip  $A$  ( $= 0.2, 0.4, 0.6$ ) and suction  $S$  ( $= 2.2, 2.3, 2.4$ ) parameters causes the velocity profile  $f'(\eta)$  to increase for the first solution, but it reduces for the second solution and for both solutions of the temperature profile  $\theta(\eta)$  as depicted in Figure 10, Figure 11, Figure 12, Figure 13, separately. For the first realizable solution, physically, the presence of velocity slip at the boundary of the shrinking surface reduces the flow resistance which causes more flow to slip through the surface and increase the flow velocity, thus a high degree of velocity slip is required to speed up the flow velocity and vice versa. For the copper volume fraction parameter  $\phi_{s2}$  ( $= 0.001, 0.005, 0.01$ ), the upsurge in value amplifies both the velocity  $f'(\eta)$  and temperature  $\theta(\eta)$  profiles for both of the solutions, as exemplified in Figures 14 and 15, but in the velocity profile  $f'(\eta)$  for the second solution, dissimilar behavior is noticed at a certain range. In Figures 16 and 17, the influences of the thermal slip parameter  $B$  ( $= 0.2, 0.4, 0.6$ ) and heat generation  $\beta$  ( $= 0.02, 0.04, 0.06$ ) parameter over the temperature profile  $\theta(\eta)$  are portrayed. Since these parameters do not affect the velocity profile  $f'(\eta)$ , it is only necessary to provide the temperature profile  $\theta(\eta)$  in this present study. The temperature profile  $\theta(\eta)$  is noticed to increase when the thermal slip parameter  $B$  decreases and when the heat generation parameter  $\beta$  increases. The appropriate amounts of thermal slip and heat generation parameters need to be controlled to obtain the required heat transfer performance, as both parameters produce a different impact that could offset each other.

As dual solutions exist, it is essential to execute the stability analysis of the flow. The stability analysis is conducted as has been discussed in the previous section. The computations of the lowest eigenvalues  $\gamma$  for  $A = 0.2$  and  $A = 0.6$  for different  $\lambda$  when  $S = 2.4$ ,  $\phi_{s2} = 0.01$ ,  $B = 0.2$  and  $\beta = 0.02$  are tabulated in Table 4. It is realized that the first solution gives the positive value of eigenvalues  $\gamma_1$ , meanwhile the second solution gives the negative value of eigenvalues  $\gamma_2$ . As according to Merkin [55] and Weidman et al. [56], the positive eigenvalues  $\gamma_1$  imply that the flow is real and stable due to the initial decay of disturbance as the time passes, and the negative eigenvalues  $\gamma_2$  imply that the flow is unreal and unstable due to the initial growth of disturbance. It is also noticeable from the table that as the value of  $\lambda \rightarrow \lambda_c$ , the value of  $\gamma \rightarrow 0$ . So, as supported by the statement

above, it can be affirmed that the flow is stable for the first solution whilst it is unstable for the second solution.

**Table 4.** The least eigenvalues for preferred values of  $A$  and  $\lambda$  as  $S = 2.4$ ,  $\phi_{s2} = 0.01$ ,  $B = 0.2$  and  $\beta = 0.02$ .

$A$	$\lambda$	Least Eigenvalues	
		First Solution ( $\gamma_1$ )	Second Solution ( $\gamma_2$ )
0.2	−1.44	0.08790	−0.08778
	−1.441	0.06126	−0.06120
	−1.4419	0.01326	−0.01326
0.6	−2.03	0.13447	−0.13450
	−2.036	0.02518	−0.02518
	−2.0362	0.00711	−0.00713

## 5. Conclusions

The slip flow of a hybrid nanofluid over a permeable exponentially stretching/shrinking sheet with the existence of heat generation has been numerically scrutinized by using the bvp4c solver. The present findings can be summarized as follows:

1. Dual solutions are achievable at the shrinking surface region as well as with the appropriate amount of suction, and only the first solution is stable.
2. The increment of the velocity slip parameter depreciates the skin friction coefficient but enhances the local Nusselt number in the shrinking surface region (first solution).
3. The skin friction coefficient is intensified (first solution) when the values of the copper volume fraction and suction parameters increase in the shrinking surface region.
4. The local Nusselt number is augmented (first and second solutions) when the copper volume fraction and suction parameters increase, but is diminished (first and second solutions) as the thermal slip and heat generation parameters increase.
5. The rise in the stretching/shrinking parameter reduces the skin friction coefficient but augments the local Nusselt number.
6. The augmentation of the velocity slip, suction and copper volume fraction parameters augments the velocity profile (first solution).
7. The temperature profile can be enhanced (first and second solutions) with the enhancement of the copper volume fraction and heat generation parameters, but can be diminished (first and second solutions) with the increment of the velocity and thermal slips and suction parameters.

**Author Contributions:** Research design, N.S.W., N.M.A., N.S.K. and I.P.; formulation and methodology, N.S.W., I.P.; result analysis, N.S.W.; validation, N.M.A. and I.P.; article preparation, N.S.W.; review and editing, N.S.W., N.M.A., N.S.K. and I.P. All authors have read and agreed to the published version of the manuscript.

**Funding:** Funded by Universiti Putra Malaysia.

**Acknowledgments:** The authors appreciatively acknowledge the support received from Ministry of Education (Malaysia) through the Fundamental Research Grant Scheme (FRGS)-5540309, Universiti Putra Malaysia and Universiti Teknikal Malaysia Melaka.

**Conflicts of Interest:** The authors declare no conflict of interest.

## Nomenclature

$u, v$	elements of velocity in $x$ and $y$ directions, respectively
$u_w$	surface velocity
$v_w$	wall mass transfer velocity
$L$	characteristic length
$\lambda$	stretching/shrinking parameter
$T$	fluid temperature
$T_w$	varying temperature of the surface
$T_\infty$	reference temperature
$q$	heat generation rate constant
$A_1$	velocity slip factor
$B_1$	thermal slip factor
$\rho_f$	fluid density
$\rho_{hnf}$	fluid density for hybrid nanofluid
$(\rho C_p)_f$	heat capacity for fluid
$(\rho C_p)_{hnf}$	heat capacity for hybrid nanofluid
$\mu_f$	dynamics viscosity for fluid
$\mu_{hnf}$	dynamics viscosity for hybrid nanofluid
$k_f$	thermal conductivity for fluid
$k_{hnf}$	thermal conductivity for hybrid nanofluid
$\phi_{s1}, \phi_{s2}$	nanoparticles volume fraction for alumina and copper, respectively
$f$	dimensionless velocity
$\theta$	dimensionless temperature
Pr	Prandtl number
$\beta$	heat generation parameter
$A$	dimensionless velocity slip parameter
$B$	dimensionless thermal slip parameter
$S$	wall mass transfer parameter
$C_f$	local skin friction coefficient
$Nu_x$	local Nusselt number
$Re_x$	local Reynolds number
$t$	time (s)
$\tau$	dimensionless time variable
$\gamma$	eigenvalue
$\gamma_1, \gamma_2$	least eigenvalue for first and second solutions, respectively

## References

1. Sidik, N.A.C.; Adamu, I.M.; Jamil, M.M.; Kefayati, G.H.R.; Mamat, R.; Najafi, G. Recent Progress on Hybrid Nanofluids in Heat Transfer Applications: A Comprehensive Review. *Int. Commun. Heat Mass Transf.* **2016**, *78*, 68–79. [[CrossRef](#)]
2. Sidik, N.A.C.; Jamil, M.M.; Japar, W.M.A.A.; Adamu, I.M. A Review on Preparation Methods, Stability and Applications of Hybrid Nanofluids. *Renew. Sustain. Energy Rev.* **2017**, *80*, 1112–1122. [[CrossRef](#)]
3. Humiric, G.; Humiric, A. Hybrid Nanofluids for Heat Transfer Applications—A State-of-the-Art Review. *Int. J. Heat Mass Transf.* **2018**, *125*, 82–103. [[CrossRef](#)]
4. Maxwell, J.C. *A Treatise on Electricity and Magnetism*; Clarendon Press: Oxford, UK, 1873.
5. Hamilton, R.L.; Crosser, O.K. Thermal Conductivity of Heterogeneous Two-Component Systems. *Ind. Eng. Chem. Fund.* **1962**, *1*, 187–191. [[CrossRef](#)]
6. Choi, S.U.S.; Eastman, J.A. Enhancing Thermal Conductivity of Fluids with Nanoparticles. *ASME Fluids Eng. Div.* **1995**, *231*, 99–106.
7. Sarkar, J.; Ghosh, P.; Adil, A. A Review on Hybrid Nanofluids: Recent Research, Development and Applications. *Renew. Sustain. Energy Rev.* **2015**, *43*, 164–177. [[CrossRef](#)]
8. Sundar, L.S.; Sharma, K.V.; Singh, M.K.; Sousa, A.C.M. Hybrid Nanofluids Preparation, Thermal Properties, Heat Transfer and Friction Factor—A Review. *Renew. Sustain. Energy Rev.* **2017**, *68*, 185–198. [[CrossRef](#)]
9. Nabil, M.F.; Azmi, W.H.; Hamid, K.A.; Zawawi, N.N.M.; Priyandoko, G.; Mamat, R. Thermo-Physical Properties of Hybrid Nanofluids and Hybrid Nanolubricants: A Comprehensive Review on Performance. *Int. Commun. Heat Mass Transf.* **2017**, *83*, 30–39. [[CrossRef](#)]
10. Sajid, M.U.; Ali, H.M. Thermal Conductivity of Hybrid Nanofluids: A Critical Review. *Int. J. Heat Mass Transf.* **2018**, *126*, 211–234. [[CrossRef](#)]

11. Babu, J.R.; Kumar, K.K.; Rao, S.S. State-of-Art Review on Hybrid Nanofluids. *Renew. Sustain. Energy Rev.* **2017**, *77*, 551–565. [[CrossRef](#)]
12. Devi, S.P.A.; Devi, S.S.U. Numerical Investigation of Hydromagnetic Hybrid Cu-Al<sub>2</sub>O<sub>3</sub>/Water Nanofluid Flow over a Permeable Stretching Sheet with Suction. *Int. J. Nonlinear Sci. Numer. Simul.* **2016**, *17*, 249–257. [[CrossRef](#)]
13. Devi, S.S.U.; Devi, S.P.A. Numerical Investigation of Three-Dimensional Hybrid Cu-Al<sub>2</sub>O<sub>3</sub>/Water Nanofluid Flow over a Stretching Sheet with Effecting Lorentz Force Subject to Newtonian Heating. *Can. J. Phys.* **2016**, *94*, 490–496. [[CrossRef](#)]
14. Devi, S.U.; Devi, S.A. Heat Transfer Enhancement of Cu-Al<sub>2</sub>O<sub>3</sub>/Water Hybrid Nanofluid Flow over a Stretching Sheet. *J. Niger. Math. Soc.* **2017**, *36*, 419–433.
15. Aly, E.H.; Pop, I. MHD Flow and Heat Transfer over a Permeable Stretching/Shrinking Sheet in a Hybrid Nanofluid with a Convective Boundary Condition. *HFF* **2019**, *29*, 3012–3038. [[CrossRef](#)]
16. Waini, I.; Ishak, A.; Pop, I. Hybrid Nanofluid Flow Induced by an Exponentially Shrinking Sheet. *Chin. J. Phys.* **2019**. [[CrossRef](#)]
17. Yashkun, U.; Zaimi, K.; Abu Bakar, N.A.; Ishak, A.; Pop, I. MHD Hybrid Nanofluid Flow over a Permeable Stretching/Shrinking Sheet with Thermal Radiation Effect. *HFF* **2020**. [[CrossRef](#)]
18. Lund, L.A.; Omar, Z.; Khan, I.; Seikh, A.H.; Sherif, E.-S.M.; Nisar, K.S. Stability Analysis and Multiple Solution of Cu-Al<sub>2</sub>O<sub>3</sub>H<sub>2</sub>O Nanofluid Contains Hybrid Nanomaterials over a Shrinking Surface in the Presence of Viscous Dissipation. *J. Mater. Res. Technol.* **2020**, *9*, 421–432. [[CrossRef](#)]
19. Lund, L.A.; Omar, Z.; Khan, I.; Sherif, E.-S.M. Dual Solutions and Stability Analysis of a Hybrid Nanofluid over a Stretching/Shrinking Sheet Executing MHD Flow. *Symmetry* **2020**, *12*, 276. [[CrossRef](#)]
20. Aladdin, N.A.L.; Bachok, N.; Pop, I. Cu-Al<sub>2</sub>O<sub>3</sub>/Water Hybrid Nanofluid Flow over a Permeable Moving Surface in Presence of Hydromagnetic and Suction Effects. *Alex. Eng. J.* **2020**, *59*, 657–666. [[CrossRef](#)]
21. Roșca, N.C.; Roșca, A.V.; Jafarimoghaddam, A.; Pop, I. Cross Flow and Heat Transfer Past a Permeable Stretching/Shrinking Sheet in a Hybrid Nanofluid. *HFF* **2020**. [[CrossRef](#)]
22. Khashi'ie, N.S.; Md Arifin, N.; Pop, I.; Nazar, R. Melting Heat Transfer in Hybrid Nanofluid Flow along a Moving Surface. *J. Therm. Anal. Calorim.* **2020**. [[CrossRef](#)]
23. Khashi'ie, N.S.; Arifin, N.M.; Pop, I.; Nazar, R.; Hafidzuddin, E.H.; Wahid, N. Flow and Heat Transfer Past a Permeable Power-Law Deformable Plate with Orthogonal Shear in a Hybrid Nanofluid. *Alex. Eng. J.* **2020**, *59*, 1869–1879. [[CrossRef](#)]
24. Khashi'ie, N.S.; Arifin, N.M.; Pop, I.; Wahid, N.S. Flow and Heat Transfer of Hybrid Nanofluid over a Permeable Shrinking Cylinder with Joule Heating: A Comparative Analysis. *Alex. Eng. J.* **2020**, *59*, 1787–1798. [[CrossRef](#)]
25. Khashi'ie, N.S.; Md Arifin, N.; Pop, I. Mixed Convective Stagnation Point Flow towards a Vertical Riga Plate in Hybrid Cu-Al<sub>2</sub>O<sub>3</sub>/Water Nanofluid. *Mathematics* **2020**, *8*, 912. [[CrossRef](#)]
26. Roy, N.C.; Pop, I. Flow and Heat Transfer of a Second-Grade Hybrid Nanofluid over a Permeable Stretching/Shrinking Sheet. *Eur. Phys. J. Plus* **2020**, *135*, 768. [[CrossRef](#)]
27. Zainal, N.A.; Nazar, R.; Naganthran, K.; Pop, I. MHD Flow and Heat Transfer of Hybrid Nanofluid over a Permeable Moving Surface in the Presence of Thermal Radiation. *HFF* **2020**. [[CrossRef](#)]
28. Anuar, N.S.; Bachok, N.; Pop, I. Radiative Hybrid Nanofluid Flow Past a Rotating Permeable Stretching/Shrinking Sheet. *HFF* **2020**. [[CrossRef](#)]
29. Gangadhar, K.; Bhargavi, D.N.; Kannan, T.; Venkata Subba Rao, M.; Chamkha, A.J. Transverse MHD Flow of Al<sub>2</sub>O<sub>3</sub>–Cu/H<sub>2</sub>O Hybrid Nanofluid with Active Radiation: A Novel Hybrid Model. *Math. Methods Appl. Sci.* **2020**, *1*–19. [[CrossRef](#)]
30. Wahid, N.S.; Md Arifin, N.; Turkyilmazoglu, M.; Hafidzuddin, M.E.H.; Abd Rahmin, N.A. MHD Hybrid Cu-Al<sub>2</sub>O<sub>3</sub>/Water Nanofluid Flow with Thermal Radiation and Partial Slip Past a Permeable Stretching Surface: Analytical Solution. *JNanR* **2020**, *64*, 75–91. [[CrossRef](#)]
31. Bataineh, K.M.; Al-Nimr, M.A. 2D Navier–Stokes Simulations of Microscale Viscous Pump With Slip Flow. *J. Fluids Eng.* **2009**, *131*, 051105. [[CrossRef](#)]
32. Sharatchandra, M.C.; Sen, M.; Gad-el-Hak, M. Thermal Aspects of a Novel Viscous Pump. *J. Heat Transf.* **1998**, *120*, 99–107. [[CrossRef](#)]
33. Nandal, J.; Kumari, S.; Rathee, R. The Effect of Slip Velocity on Unsteady Peristalsis MHD Blood Flow through a Constricted Artery Experiencing Body Acceleration. *Int. J. Appl. Mech. Eng.* **2019**, *24*, 645–659. [[CrossRef](#)]
34. Andersson, H.I. Slip Flow Past a Stretching Surface. *Acta Mechanica* **2002**, *158*, 121–125. [[CrossRef](#)]
35. Hayat, T.; Nadeem, S.; Khan, A.U. Rotating Flow of Ag-CuO/H<sub>2</sub>O Hybrid Nanofluid with Radiation and Partial Slip Boundary Effects. *Eur. Phys. J. E* **2018**, *41*, 75. [[CrossRef](#)]
36. Nadeem, S.; Abbas, N. On Both MHD and Slip Effect in Micropolar Hybrid Nanofluid Past a Circular Cylinder under Stagnation Point Region. *Can. J. Phys.* **2019**, *97*, 392–399. [[CrossRef](#)]
37. Muhammad, K.; Hayat, T.; Alsaedi, A.; Ahmad, B.; Momani, S. Mixed Convective Slip Flow of Hybrid Nanofluid (MWCNTs + Cu + Water), Nanofluid (MWCNTs + Water) and Base Fluid (Water): A Comparative Investigation. *J. Therm. Anal. Calorim.* **2020**. [[CrossRef](#)]
38. Yan, L.; Dero, S.; Khan, I.; Mari, I.A.; Baleanu, D.; Nisar, K.S.; Sherif, E.-S.M.; Abdo, H.S. Dual Solutions and Stability Analysis of Magnetized Hybrid Nanofluid with Joule Heating and Multiple Slip Conditions. *Processes* **2020**, *8*, 332. [[CrossRef](#)]
39. Alharbi, S.O. Influence of Wall Slip and Jump in Wall Temperature on Transport of Heat Energy in Hybrid Nanofluid. *J. Therm. Anal. Calorim.* **2020**, *1*–8. [[CrossRef](#)]

40. Tlili, I.; Khan, W.A.; Khan, I. Multiple Slips Effects on MHD SA-Al<sub>2</sub>O<sub>3</sub> and SA-Cu Non-Newtonian Nanofluids Flow over a Stretching Cylinder in Porous Medium with Radiation and Chemical Reaction. *Results Phys.* **2018**, *8*, 213–222. [[CrossRef](#)]
41. Aly, E.H.; Pop, I. MHD Flow and Heat Transfer near Stagnation Point over a Stretching/Shrinking Surface with Partial Slip and Viscous Dissipation: Hybrid Nanofluid versus Nanofluid. *Powder Technol.* **2020**, *367*, 192–205. [[CrossRef](#)]
42. Eid, M.R.; Nafe, M.A. Thermal Conductivity Variation and Heat Generation Effects on Magneto-Hybrid Nanofluid Flow in a Porous Medium with Slip Condition. *Waves Random Complex Media* **2020**, *1*–25. [[CrossRef](#)]
43. Abbas, Z.; Naveed, M.; Sajid, M. Hydromagnetic Slip Flow of Nanofluid over a Curved Stretching Surface with Heat Generation and Thermal Radiation. *J. Mol. Liquids* **2016**, *215*, 756–762. [[CrossRef](#)]
44. Upreti, H.; Pandey, A.K.; Kumar, M. MHD Flow of Ag-Water Nanofluid over a Flat Porous Plate with Viscous-Ohmic Dissipation, Suction/Injection and Heat Generation/Absorption. *Alex. Eng. J.* **2018**, *57*, 1839–1847. [[CrossRef](#)]
45. Jusoh, R.; Nazar, R.; Pop, I. Impact of Heat Generation/Absorption on the Unsteady Magnetohydrodynamic Stagnation Point Flow and Heat Transfer of Nanofluids. *HFF* **2019**, *30*, 557–574. [[CrossRef](#)]
46. Murugesan, T.; Kumar, M.D. Effects of Thermal Radiation and Heat Generation on Hydromagnetic Flow of Nanofluid over an Exponentially Stretching Sheet in a Porous Medium with Viscous Dissipation. *World Sci. News* **2019**, *128*, 130–147.
47. Hayat, T.; Nadeem, S. Heat Transfer Enhancement with Ag–CuO/Water Hybrid Nanofluid. *Results Phys.* **2017**, *7*, 2317–2324. [[CrossRef](#)]
48. Hayat, T.; Nadeem, S.; Khan, A.U. Numerical Analysis of Ag–CuO/Water Rotating Hybrid Nanofluid with Heat Generation and Absorption. *Can. J. Phys.* **2019**, *97*, 644–650. [[CrossRef](#)]
49. Ghosh, S.; Mukhopadhyay, S. Stability Analysis for Model-Based Study of Nanofluid Flow over an Exponentially Shrinking Permeable Sheet in Presence of Slip. *Neural Comput. Appl.* **2020**, *32*, 7201–7211. [[CrossRef](#)]
50. Mukhopadhyay, S.; Andersson, H.I. Effects of Slip and Heat Transfer Analysis of Flow over an Unsteady Stretching Surface. *Heat Mass Transf.* **2009**, *45*, 1447–1452. [[CrossRef](#)]
51. Tayebi, T.; Chamkha, A.J. Entropy Generation Analysis during MHD Natural Convection Flow of Hybrid Nanofluid in a Square Cavity Containing a Corrugated Conducting Block. *HFF* **2019**, *30*, 1115–1136. [[CrossRef](#)]
52. Takabi, B.; Salehi, S. Augmentation of the Heat Transfer Performance of a Sinusoidal Corrugated Enclosure by Employing Hybrid Nanofluid. *Adv. Mech. Eng.* **2015**, *6*, 147059. [[CrossRef](#)]
53. Ghalambaz, M.; Roșca, N.C.; Roșca, A.V.; Pop, I. Mixed Convection and Stability Analysis of Stagnation-Point Boundary Layer Flow and Heat Transfer of Hybrid Nanofluids over a Vertical Plate. *Int. J. Numer. Methods Heat Fluid Flow* **2019**, *30*, 3737–3754. [[CrossRef](#)]
54. Oztop, H.F.; Abu-Nada, E. Numerical Study of Natural Convection in Partially Heated Rectangular Enclosures Filled with Nanofluids. *Int. J. Heat Fluid Flow* **2008**, *29*, 1326–1336. [[CrossRef](#)]
55. Merkin, J.H. On Dual Solutions Occurring in Mixed Convection in a Porous Medium. *J. Eng. Math.* **1986**, *20*, 171–179. [[CrossRef](#)]
56. Weidman, P.D.; Kubitschek, D.G.; Davis, A.M.J. The Effect of Transpiration on Self-Similar Boundary Layer Flow over Moving Surfaces. *Int. J. Eng. Sci.* **2006**, *44*, 730–737. [[CrossRef](#)]
57. Hafidzuddin, M.E.H.; Nazar, R.; Arifin, N.M.; Pop, I. Boundary Layer Flow and Heat Transfer over a Permeable Exponentially Stretching/Shrinking Sheet with Generalized Slip Velocity. *JAFM* **2016**, *9*, 2025–2036. [[CrossRef](#)]